AIAA JOURNAL
Vol. 46, No. 4, April 2008

Direct Noise Computation of the Turbulent Flow Around a Zero-Incidence Airfoil

Olivier Marsden,* Christophe Bogey,† and Christophe Bailly‡
Ecole Centrale de Lyon, 69134 Ecully France

DOI: 10.2514/1.29825

A large eddy simulation of the flow around a NACA 0012 airfoil at zero incidence is performed at a chord-based Reynolds number of 500,000 and a Mach number of 0.22. The aim is to show that high-order numerical schemes can successfully be used to perform direct acoustic computations of compressible transitional flow on curvilinear grids. At a Reynolds number of 500,000, the boundary layers around the airfoil transition from an initially laminar state to a turbulent state before reaching the trailing edge. Results obtained in the large eddy simulation show a well-placed transition zone and turbulence levels in the boundary layers that are in agreement with experimental data. Furthermore, the radiated acoustic field is determined directly by the large eddy simulation, without the use of an acoustic analogy. Third-octave acoustic spectra are compared favorably with experimental data.

Nomenclature

C_f	=	skin-friction coefficient, $\tau_f/(0.5\rho U_\infty^2)$
C_p	=	mean-pressure coefficient, $(p - p_\infty)/(0.5\rho U_\infty^2)$
c	=	chord length of the airfoil
c_0	=	sound speed in the medium at rest
H	=	boundary-layer shape factor, δ^*/δ_θ
M	=	Mach number, U_∞/c_0
Re_c	=	Reynolds number based on the airfoil chord, $U_\infty c/\nu$
Re_θ	=	Reynolds number based on the momentum thickness
t_c	=	convection time across the airfoil, c/U_∞
U_∞	=	upstream flow velocity
u_τ	=	wall-friction velocity $u_\tau = \sqrt{\tau_f/\rho}$
u', v', w'	=	velocity fluctuations
δ_*	=	boundary-layer displacement thickness
δ_θ	=	boundary-layer momentum thickness
η^+, z^+	=	wall-unit curvilinear coordinates
μ	=	molecular viscosity
ν	=	dynamic viscosity, μ/ρ
ξ^+	=	wall-unit curvilinear coordinate, $\xi u_\tau/\nu$
τ_f	=	wall shear, $\mu\partial u/\partial\eta|_{y=0}$

I. Introduction

RECENT rapid advances in computational aeroacoustics have greatly increased the scope of problems that can be tackled by numerical methods. This is particularly true of direct noise computations, in which the sound waves generated by turbulent flows are obtained directly from an unsteady compressible simulation of the Navier–Stokes equations. Such simulations require great attention to numerical detail, because propagative acoustic fluctuations generally have energy levels that are several orders of magnitude inferior to those of the aerodynamic flow features, and they have wavelengths that are orders of magnitude larger than those of the flow features. Moreover, acoustic propagation distances are often large in comparison with the extent of the source-containing unsteady flow region.

The simulation of high-Reynolds-number flows is now increasingly feasible, due to the development of high-order large eddy simulation (LES) approaches that manage to preserve the small-amplitude acoustic perturbations alongside the larger-amplitude aerodynamic fluctuations over a wide range of wave numbers. Both explicit schemes such as Tam and Webb's [1] dispersion-relation-preserving scheme or those proposed by Bogey and Bailly [2] and implicit schemes such as Padé-type schemes [3,4] have been successfully applied to aeroacoustic simulations at high Reynolds numbers. The field of jet aeroacoustics has been particularly active in the advancement of these techniques, and a number of high-Reynolds-number jet flow simulations can be found in the literature [5–8].

More recently, work on high-accuracy computations around curved geometries has shown that high-precision methods are not restricted to simulations around Cartesian geometries [9–12]. Cylinders and airfoils have so far been the most-studied curved geometries, due to the large amount of experimental data available and the fundamental academic interest that they present. A number of time-accurate numerical studies have been performed around airfoils, often placed at a small angle of attack to the flow and generally using an acoustic analogy to obtain far-field sound characteristics [10,13–16].

Wang and Moin [13] studied the turbulent flow around the trailing edge of a Blake airfoil at a chord-based Reynolds number of $Re_c = 2.15 \times 10^6$. The incompressible flow data were used to calculate far-field acoustic information using an integral formulation of Lighthill's equation [17], by approximating the airfoil's Green function by that of an infinitely thin flat plate. They found a reasonable agreement between their computed acoustic field and Blake's [18] experimental results for high frequencies, but low-frequency values were badly estimated, due to the insufficient transversal extent of their computational domain. Manoha et al. [10] performed an LES simulation around a NACA 0012 airfoil at a chord-based Reynolds number of $Re_c = 2.86 \times 10^6$, placed at 5 deg of incidence to the incoming flow. A Kirchhoff formulation was used to calculate the acoustic far field. Oberai et al. [14] simulated the incompressible flow around an Eppler 387 airfoil at a Reynolds number of $Re_c = 1 \times 10^5$ and used the results as an input to a variational form of Lighthill's equation for the computation of the acoustic far field. They then studied the acoustic directivity of the scattered pressure as a function of frequency and observed, as

Presented as Paper 2007-2503 at the 12th AIAA/CEAS Aeroacoustics Conference, Cambridge, MA, 8–10 May 2006; received 17 January 2007; revision received 19 November 2007; accepted for publication 22 November 2007.

*Assistant Professor, Laboratoire de Mécanique des Fluides et d'Acoustique, Unite Mixte de Recherche, 5509 du Centre National de la Recherche Scientifique; Olivier.Marsden@ec-lyon.fr.

†Research Scientist, Laboratoire de Mécanique des Fluides et d'Acoustique, Unite Mixte de Recherche, 5509 du Centre National de la Recherche Scientifique; Christophe.Bogey@ec-lyon.fr.

‡Professor, Laboratoire de Mécanique des Fluides et d'Acoustique, Unite Mixte de Recherche, 5509 du Centre National de la Recherche Scientifique; Christophe.Bailly@ec-lyon.fr.

expected, dipolelike radiation for large wavelengths and more complex lobed diffraction patterns for wavelengths shorter than the airfoil chord.

High-order Navier–Stokes finite difference simulations have proved their value in the study of noise-generation mechanisms for Cartesian geometries such as free jet flows and rectangular cavity flows [19]. We are thus attempting to develop similar methods for more complex curved geometries. Our aim is to show that it is possible to generate accurate descriptions of the turbulent compressible flow around complex geometries while simultaneously obtaining realistic noise-level estimations without making use of acoustic analogies or other split source–propagation techniques, which incur problems of their own. The current work describes the development and use of a parallel curvilinear solver based on high-order methods to study the compressible flow around a 3-D NACA 0012 airfoil at a chord-based Reynolds number of 500,000, placed at zero incidence to the upstream flow. It focuses on showing that realistic compressible boundary-layer transition is captured without needing to trigger the transition artificially, even when the airfoil is placed at zero incidence to the upstream flow. Both mean flow quantities and fluctuation statistics are compared with results available in the literature. The acoustic field generated by the airfoil is also examined, and spectra computed from the pressure field are compared with experimental data.

II. Numerical Aspects

The full 3-D Navier–Stokes equations are solved on a structured computational grid that is obtained from a body-fitted C-type grid by applying a suitable coordinate transform. Details on the equations themselves can be found in Appendix A. The transformed equations are resolved on the computational grid with an optimized high-order numerical procedure. Viscous terms in these equations are computed by successive first derivatives. Away from boundaries, spatial discretization is performed with explicit 11-point centered finite differences optimized to minimize dispersion for wave numbers discretized by between 4 and 32 grid points [2]. Close to boundaries, be they solid walls or radiation conditions, optimized explicit noncentered differencing schemes are used [20]. The noncentered differencing schemes are all based on 11-point stencils, including the one-sided stencil used for wall points. Time integration is performed with a six-step second-order optimized low-storage Runge–Kutta algorithm [2]. Characteristics regarding dispersion and dissipation for the spatial differencing schemes, filters, and the time-integration scheme can be found in previous papers [2,20]. This solver has been validated on reference flow configurations and on a demanding multibody acoustic scattering test case, yielding results in good agreement with experimental and analytical data [12].

The schemes' properties mean that the behavior of waves discretized by at least four points per wavelength is accurately reproduced, with very low levels of dispersion and dissipation for frequencies such that $\omega\Delta t \leq 1.25 \times \pi$. The determination of the time step is based on a Courant–Friedrichs–Lewy (CFL) criterion,

$$\mathrm{CFL} = \frac{(U_\infty + c_0)\Delta t}{\Delta x} = 0.85$$

where Δx is the smallest grid spacing in the computational grid. The airfoil wall is modeled as an isothermal nonslip boundary, which is based entirely on the use of the noncentered schemes described previously. The wall-point density and pressure are updated by resolving the governing equations in curvilinear form, in which all terms containing wall velocities are eliminated using high-order noncentered differencing schemes, as described in Appendix A. This boundary condition formulation is inherently capable of dealing with meshes that are not orthogonal to the wall boundary, because the nonperpendicular nature of the grid is taken into account via the Jacobian matrix. It thus reduces potential orthogonality problems near the trailing edge and allows the use of a grid with superposed points in the wake zone, as illustrated in Fig. 1. By the use of such a grid, it is possible to maintain a continuous variation of three of the four terms in the Jacobian matrix used in the transformed

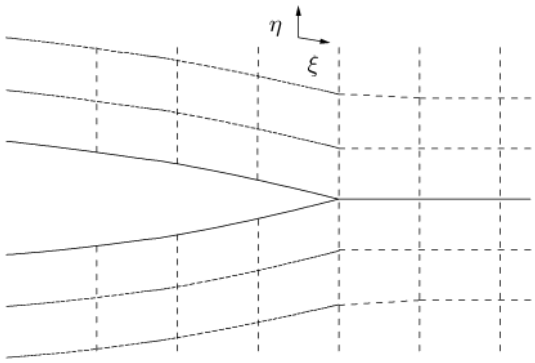

Fig. 1 Close-up view of the nonorthogonal grid around the trailing edge of the NACA 0012 airfoil.

Navier–Stokes equations. Only the term $\partial\eta/\partial y$ as a function of x is discontinuous by construction at the trailing edge. The superposed grid points in the wake zone allow this area to be treated as an inner grid zone. In particular, along the wake line (shown as the solid horizontal line to the right of the trailing edge in Fig. 1), all terms of the grid metrics are computed with the 11-point centered finite differences.

Filtering is of crucial importance in this solver. Indeed, its role is not only to remove spurious grid-to-grid oscillations that can arise (for example, from meshing imperfections), but also to act as a subgrid-scale model instead of the more commonly used eddy-viscosity models. The action of the finest turbulent scales is assumed to be limited to dissipation, and their effect is then modeled by removing high-frequency energy in a highly controlled fashion. In practice, this is done by applying a specific selective filtering procedure to the flow variables at each time-step. The explicit 11-point filtering stencil is designed to remove fluctuations discretized by less than four grid points per wavelength, leaving all larger wavelengths effectively untouched [2]. This LES approach has been successfully used to examine isotropic turbulence [21], channel flow [22], and jet noise [23,24]. Because the differencing schemes used near boundaries are asymmetric, their effective wave numbers have an imaginary part that leads to them being unstable for very high frequencies [25]. It is therefore essential to use them in conjunction with appropriate highly selective filters and, to this end, we use the filters described in Berland et al. [20], which also selectively damp fluctuations with fewer than four points per wavelength. Filters for grid points more than two points away from a boundary are built on 11-point stencils, whereas the last- and second-last-point stencils up to two points away from a boundary are built, respectively, on four and seven points. Thus, at the wall, the centered 11-point filter is used in the ξ and ζ directions, whereas the family of noncentered filters is applied in the η direction. The boundary condition in the spanwise direction is periodic and is implemented in such a way as to allow the use of the 11-point differencing and filter stencils up to the lateral boundaries. At the lateral radiation boundaries in the η and ξ directions, a three-dimensional generalization of Tam and Dong's [26] 2-D far-field radiation condition is used. Details on the 3-D formulation can be found in Bogey and Bailly [27]. Finally, the incoming flow is imposed as uniform.

Examples of 2-D acoustic diffraction and aeroacoustic flows successfully simulated with the solver described in this work can be found in Marsden et al. [12]. Parallelization of the code is based on the MPI interface. The computational domain is split along the radial and circumferential directions, resulting in a number of structured subdomains that communicate along their shared boundaries at each subiteration of the Runge–Kutta time-integration procedure. No dynamic load balancing is performed, but given the structure of the code, an equal number of points in each zone leads to reasonably similar computational costs for each zone. Communication is performed such that the 11-point differencing scheme and filters can be applied transparently and in a time-accurate manner [28] right up to each boundary separating adjacent subdomains. An evaluation of the communication overheads performed on a cluster of Alpha EV7

processors with a high-speed Infiniband™ interconnect showed that communication overheads remained under 5% of the total computational time for the grid used in this work and for numbers of processors ranging up to 126.

The computation presented here describes the flow around a 3-D NACA 0012 airfoil placed at zero incidence to a flow at a Mach number of $M = 0.22$. The airfoil has a chord of $c = 10$ cm and the resulting chord-based Reynolds number is $Re_c = 5 \times 10^5$. The computation was performed on a 12.3-million point grid, composed of 1193 points in the circumferential direction, 230 points in the radial direction, and 45 points in the spanwise direction. The computational domain is split into 13 subdomains, and the parallel computation was run on a laboratory cluster of 13 AMD Opteron processors linked by a standard gigabit Ethernet network. The computation was run for a total of 10^6 iterations, of which the first 400,000 were discarded and the last 600,000 were used to compute the statistics reported in this work. These 600,000 iterations correspond to 15 airfoil flow-through times based on the upstream velocity U_∞. The total computational wall time was approximately 4000 h. Grid resolution is important for such a simulation, if one is to capture the detailed boundary-layer behavior without using wall models. Indeed, various studies [29–31] performed in the European project titled LESFOIL (large eddy simulation of the flow around an airfoil) have concluded that low grid resolution leads to poor computational results when transitional phenomena are present. Furthermore, these studies showed that different subgrid-scale models tend to show widely varying results on under-resolved transitional zones, due perhaps to the subgrid-scale viscosity adversely affecting laminar flow regions. Therefore, in this work, care is taken to ensure that near-wall grid resolution is satisfactory. Grid spacings in wall units close to the trailing edge are as follows: $\xi^+ \simeq 20$, $\eta^+ \simeq 2.5$, and $z^+ \simeq 20$ in the streamwise, radial, and spanwise directions, respectively. The total computational domain extends out approximately one chord length in the radial direction and half a chord length beyond the trailing edge in the downstream direction, and the spanwise extent of the grid corresponds to approximately 5% of the airfoil's chord length.

A sponge zone is used in the last 20 points of the wake zone to minimize the force of vortical structures impinging on the downstream radiation condition. The sponge zone is implemented by the combination of strong grid stretching (on the order of 10% between adjacent grid cells) and an additional Laplacian-type dissipation term.

III. Results

A. Mean Flowfield

The pressure distribution around the airfoil is an important parameter, both in terms of aerodynamic characteristics (because it determines the lift and drag coefficients of the airfoil) and in terms of boundary-layer behavior (because the pressure gradient is known to affect the development of both laminar and turbulent boundary layers [32,33]). This distribution is shown in Fig. 2 and is compared with experimental values obtained by Lee and Kang [34] for a NACA 0012 airfoil at a chord-based Reynolds number of 600,000 and a Mach number of $M = 0.09$. A good agreement is found between the computational and experimental results. Of importance is the fact that from $x/c = 0.15$ down to the trailing edge, the boundary layer is subject to an adverse pressure gradient.

Results concerning the boundary-layer transition from a laminar to a turbulent state are now examined. It should be noted that transition is a very sensitive flow phenomenon and, as such, can be strongly affected by experimental conditions (in particular, the level of freestream turbulence [35,36]). Thus, experimental results regarding transition show spread, and qualitative agreement between the computation and experimental results is already a challenging goal. As an illustration of this, experimental transition results from similar configurations at relatively low Reynolds numbers are gathered in Table 1. A good reference for higher Reynolds numbers can be found in [38].

In the present simulation, the position of what might be loosely referred to as the *instantaneous transition zone* varies slightly with time, at a very low rate (substantially lower than the frequencies associated with most flow events in the boundary layer), because its Strouhal number based on the airfoil thickness is on the order of $St_c = 0.016$. Over the total physical simulation time during which data were collected, only approximately two oscillations of the transition location were observed, and so the regularity of this phenomenon could not be ascertained. The beginning of the transition zone appears to move roughly between $x/c = 0.4$ and 0.55, whereas the end of the zone oscillates between $x/c = 0.7$ and 0.8. These observed bounds are very approximate by nature: first, because only two cycles of the oscillation have been observed, and second, because it is hard to give a clean definition of an instantaneous transition zone. It is believed that this oscillation is not due to a lack of convergence of the computation, but its origin remains unclear. It appears not to be imputable to a global oscillation of the whole computational domain, because the velocity field near the upstream and lateral boundary conditions shows no sign of comparable fluctuations, and the pressure field oscillates by around 1 Pa, which should not sufficient to lead to the observed boundary-layer behavior. It is also hard to know whether this oscillation is physical or not, because experimental data sufficiently resolved at very low frequencies have not been found. Unless otherwise specified, boundary-layer data presented in this work are averaged over the entire physical part of the run.

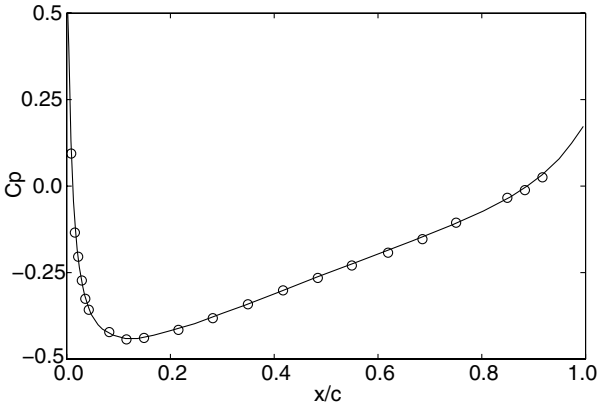

Fig. 2 Mean-pressure coefficient $C_p = (p - p_\infty)/(0.5\rho u_\infty^2)$ around a NACA 0012 airfoil: Lee and Kang [34] measurements at $Re_c = 600,000$ (○) and simulation results at $Re_c = 5 \times 10^5$ and $M = 0.22$ (solid line).

A first illustration of the boundary-layer behavior is shown in Fig. 3. Mean velocity profiles at different points along the chord are represented according to inner-region scalings [i.e., $u^+ = f(y^+)$]. Typical laminar boundary-layer behavior is observed up to $x/c = 0.52$, where $u^+ = y^+$ (shown in dashes in Fig. 3) over the viscous sublayer thickness. Downstream of the point $x/c = 0.52$, velocity profiles deviate from the viscous $u^+ = y^+$ law at a distance of roughly 10 wall units from the wall. The velocity profile around the end of the transition region at $x/c = 0.71$ exhibits a viscous sublayer until approximately $y^+ = 10$. From $y^+ \simeq 10$ to around $y^+ \simeq 80$, the profile approximately follows the standard logarithmic law $u^+ = (1/\kappa)\,\ell_n\, y^+ + B$ established for a zero-pressure-gradient boundary layer (dashed line in Fig. 3, with $1/\kappa$ and B taking the standard values of 2.44 and 5.2), albeit being slightly above, which is consistent with the adverse pressure gradient faced by the boundary layer and is also observed in the experimental data of Lee and Kang [34]. It is in fact possible to derive a similar logarithmic law governing the mean velocity in the overlap region when the pressure

Table 1 Transition positions for various experimental works on the flow around an airfoil at zero incidence

Gartenberg and Roberts [39]	$Re_c = 3.7 \times 10^5$	$x/c \simeq 0.8$
Lee and Kang [34]	$Re_c = 6 \times 10^5$	$0.62 \leq x/c \leq 0.78$
Kerho and Bragg [37]	$Re_c = 7.5 \times 10^5$	$0.65 \leq x/c \leq 0.77$
	$Re_c = 1.25 \times 10^6$	$0.57 \leq x/c \leq 0.67$
	$Re_c = 2.25 \times 10^6$	$0.43 \leq x/c \leq 0.50$

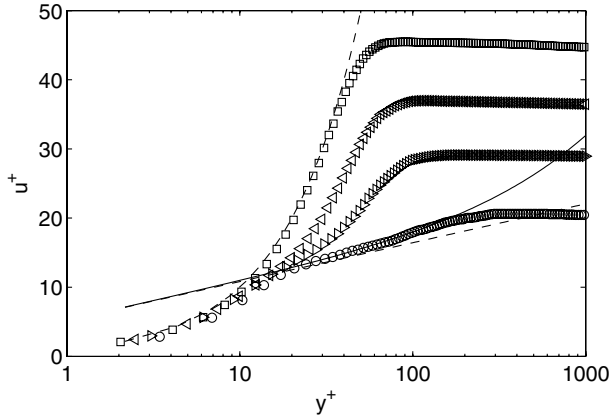

Fig. 3 Velocity profiles plotted in wall units $u^+ = f(y^+)$ in the upper boundary layer around the NACA 0012 airfoil at $Re_c = 5 \times 10^5$ and $M = 0.22$; x/c simulation results are 0.52 (□), 0.58 (◁), 0.63 (▷), and 0.75 (○), and u^+ theoretical curves are y^+ (dashed line), $2.44 \log(y^+) + 5.2$ (dashed line), and $f(y^+, \lambda)$ (solid line) [see Eq. (1)].

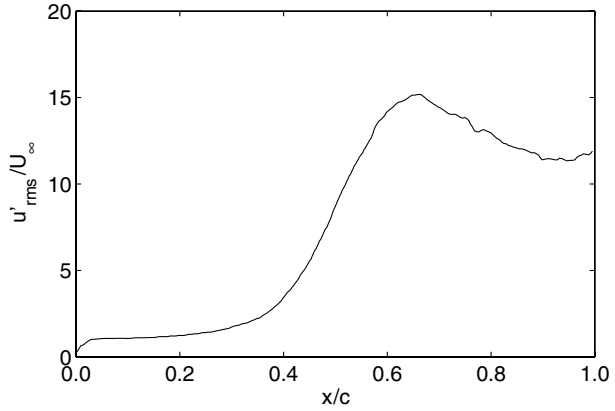

Fig. 4 Velocity fluctuations $u'_{\mathrm{rms}}/U_\infty$ in the upper boundary layer around the NACA 0012 airfoil at $Re_c = 5 \times 10^5$ and $M = 0.22$, calculated at $y^+ \simeq 16$ and plotted as a function of x/c.

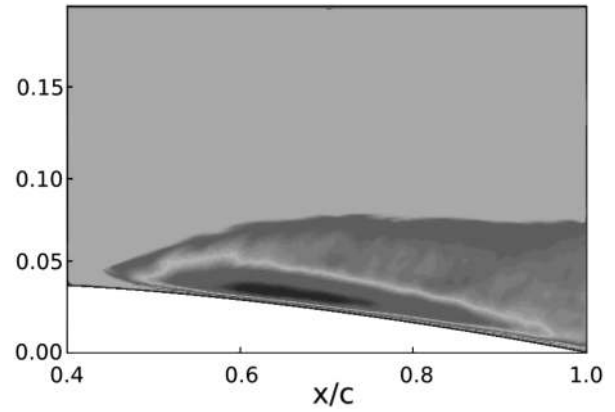

Fig. 5 View of the rms streamwise velocity fluctuations around the transition zone on the NACA 0012 airfoil at $Re_c = 5 \times 10^5$ and $M = 0.22$; gray to black is between 0 and 15% of the freestream velocity; vertical scale is dilated by a factor of 10.

gradient cannot be neglected. Following Afzal's approach [40], the effect of an adverse pressure gradient on u^+ in the overlap zone can be taken into account by

$$u^+ = \frac{1}{\kappa}\left(\ell_n\, y^+ - 2\,\ell_n \frac{\sqrt{1+\lambda y^+}+1}{2} + 2(\sqrt{1+\lambda y^+}-1)\right) + B \tag{1}$$

where

$$\lambda = \left(\frac{u_p}{u_\tau}\right)^3 \quad \text{and} \quad u_p = \left(\frac{\nu}{\rho}\frac{\mathrm{d}P}{\mathrm{d}x}\right)^{1/3}$$

This expression is computed with the streamwise pressure gradient obtained in the computation and is represented in Fig. 3 with the solid line. A much better fit is found with the velocity profile at $x/c = 0.71$ obtained from the computation. Inside the transition zone, velocity profiles are neither laminar, because mean velocity increases less than linearly with the distance from the wall, nor are they fully turbulent. In fact, the velocity profiles appear to sweep the entire domain between the linear law and the logarithmic law as transition takes place, as also observed experimentally by Lee and Kang [34].

The shape factor at the trailing edge is found to be $H = \delta^*/\delta_\theta \simeq 2$, below typical values at which turbulent boundary-layer separation is observed experimentally. The momentum-thickness-based Reynolds number is $Re_\theta = 980$, to be compared with the value of slightly above 1000 found experimentally by Lee and Kang [34].

B. Flow Fluctuation Statistics

Figure 4 represents rms turbulent streamwise velocity fluctuations measured at a height of $y^+ = 16$ along the upper boundary layer of the airfoil, plotted as a percentage of the freestream velocity. The level of fluctuations starts to increase notably around $x/c = 0.45$, and it increases rapidly to reach a saturation level of approximately 15% of freestream velocity, at roughly $x/c = 0.65$. Their level then diminishes slightly and flattens out between $x/c \simeq 0.8$ and the trailing edge. The transition region thus commences in the vicinity of $x/c = 0.45$. It can be noted, however, that the level of fluctuations before the transition zone is not zero. There are indeed velocity fluctuations in the boundary layer in this region, as will be seen later, but their level does not increase. The end of the transition zone is presumably close to the location after which the level of fluctuations is approximately constant, but the information given by this plot is not sufficient to place the zone's end with precision. However, these preliminary values are in good agreement with experimental data. For example, Lee and Kang [34] found the transition zones around a NACA 0012 airfoil at a Reynolds number of 600,000 and zero angle of attack to be located between $x/c = 0.62$ and 0.78 using measurements performed by hot-wire anemometry. The transition zones are shorter than those on a flat plate at an equivalent Reynolds number because of the presence of an adverse pressure gradient in this region created by the airfoil's geometry.

Figure 5 shows a grayscale-map view of the rms streamwise velocity fluctuations around the transition zone. The vertical scale in this figure has been dilated by a factor of 10 to better show the region of interest. It can be seen in this view that the maximum levels of fluctuations are located between $x/c = 0.6$ and 0.75, which confirms the previous estimation of the transition zone's extent. It can also be noted that the zone of maximum rms fluctuations is located quite close to the airfoil's surface, in the first third of the boundary-layer thickness. This view of the rms fluctuations is in good qualitative agreement with similar plots presented by Kerho and Bragg [37] for a smooth NACA 0012 airfoil at a Reynolds number of $Re_c = 750,000$ and a Mach number of $M = 0.062$.

A better indication of the extent of the transition zone can be obtained from the variation in the local skin-friction coefficient $C_f = \tau_w/(0.5\rho U_\infty^2)$. Indeed, the skin-friction coefficient in the laminar zone for a flat plate follows a different law from that in a turbulent zone. Figure 6a shows the skin-friction coefficient obtained in this computation for the central zone of the airfoil from 30 to 90% of the chord.

The minimum skin friction is reached around $x/c = 0.5$, after which point it rises rapidly to attain a maximum at about $x/c = 0.72$ before decreasing again toward the trailing edge. This places the transition zone's upstream and downstream bounds at $x/c \simeq 0.5$ and $\simeq 0.72$, respectively. The minimum value of $C_f \simeq 1.3 \times 10^{-3}$ computed from the simulation results is higher than that of approximately 7.5×10^{-4} observed by Lee and Kang [34], but this is

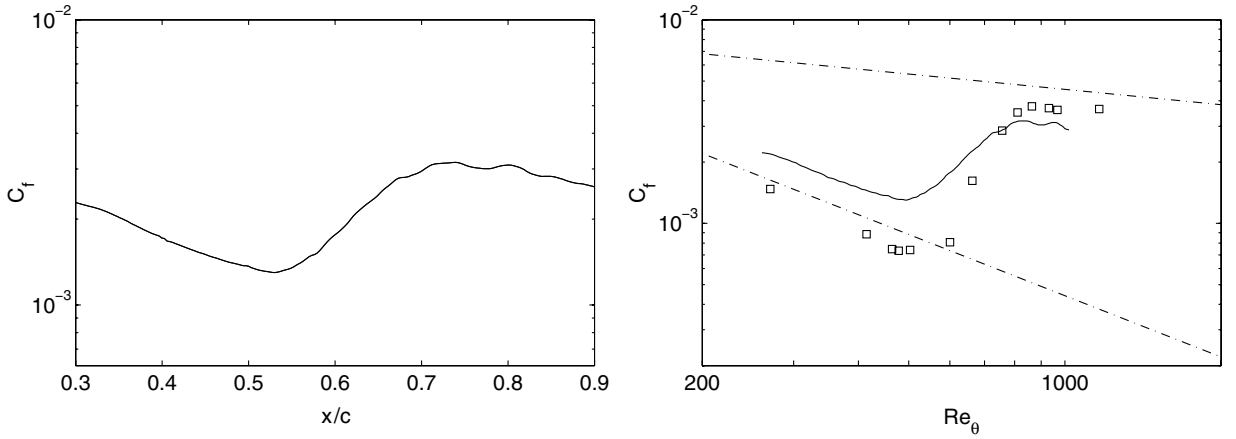

a) b)

Fig. 6 Skin friction a) $C_f = \tau_w/(0.5\rho U_\infty^2)$ around the transition zone of the NACA 0012 airfoil at $Re_c = 5 \times 10^5$ and $M = 0.22$ and b) as a function of momentum-based Reynolds number Re_θ (solid line), experimental data from Lee and Kang [34] (□), and laminar variation $C_f = 0.4409/Re_\theta$ and turbulent variation $C_f = 0.0256/Re_\theta^{1/4}$ (dashed line).

due at least in part to the slowly varying position of the transition zone, which has a tendency to flatten out the average skin-friction curve. Similarly, the maximum computed value of $C_f \simeq 3.2 \times 10^{-3}$ is lower than the experimentally observed value of almost 4×10^{-3}. The computed skin-friction coefficient is represented in Fig. 6b as a function of the momentum-thickness-based Reynolds number and is compared with that measured by Lee and Kang. Classical expressions [41] for C_f variation in laminar and turbulent regimes are also represented by the dashed lines. The minimum skin-friction value is obtained for $Re_\theta = 500$ and the maximum is attained around $Re_\theta = 800$. These Reynolds numbers are similar to those of $Re_\theta =$ 500 and 860 observed by Lee and Kang [34]. The slopes observed in both the laminar and turbulent zones also compare reasonably well; however, the skin-friction coefficient is overestimated by around 40% in the laminar zone and underestimated by approximately 20% in the turbulent region of the boundary layer. The reason for these large discrepancies is not known.

The rms fluctuation profiles of streamwise velocity as a function of distance from the wall are shown in Figs. 7a and 7b, computed at different points from the laminar zone down to the turbulent region. They are compared with those obtained experimentally by Lee and Kang [34]. Computed profiles have not been plotted at exactly the experimental streamwise locations, but the closest fit to each experimental profile has been represented instead, along with its corresponding location. Reasonable qualitative agreement in turbulent fluctuation profiles is found between computational results and those obtained by Lee and Kang, although the computational values are all higher than the experimental data. The overestimation is of approximately 40% in the early stages of transition and approximately 15% once the transition is completed. The 15% overshoot in velocity fluctuations in the turbulent region is roughly consistent with the 20% deficit in the computed skin-friction coefficient in the same region, on which the velocity scale is based with the relation $u_\tau = \sqrt{\tau_f/\rho}$. The cause of the overestimation in the early stages of transition might be due in part to the application of periodic boundary conditions in the spanwise direction. Indeed, the spanwise correlation length in the transitional zone, although not given by Lee and Kang, is undoubtedly larger than the computational domain. The periodic boundary conditions will therefore have a tendency to strengthen the two-dimensional aspect of the flow in this area, which can lead to an increase in the fluctuation intensities. This is no longer the case downstream of the transition zone, because correlation lengths in the turbulent region are much smaller. As an indication, the integral streamwise length scale in the turbulent region is on the order of 7×10^{-4} m just upstream of the trailing edge, to be compared with the 5-mm spanwise extent of the computational domain.

It can be noticed that as the maximum fluctuation level rises in the first part of the transition zone, the height of the maximum also increases, which would tend to indicate that the vortical structures in this region climb progressively through the boundary layer, in keeping with traditional zero-pressure-gradient transition

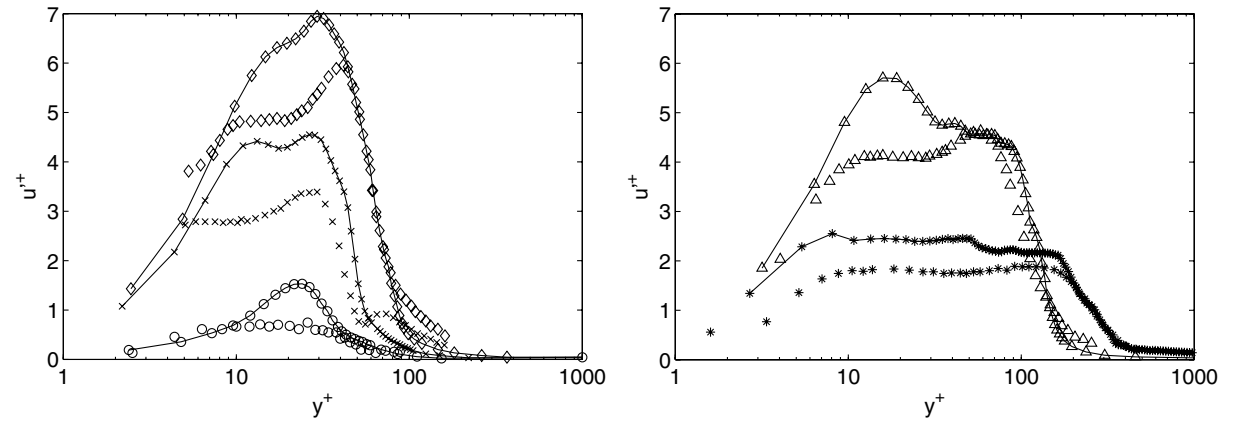

a) b)

Fig. 7 □◁▷○△◇★Comparison of x/c velocity fluctuation profiles in the upper boundary layer around a NACA 0012 airfoil: a) computed values are 0.4 (-○-), 0.58 (-×-), and 0.63 (-◇-), and experimental values are 0.45 (○), 0.62 (×, and 0.65 (◇); b) computed values are 0.69 (-△-) and 0.85 (-★-), and experimental values are 0.68 (△) and 0.78 (★).

scenarios [42]. The maximum value of $u'^{+}_{\mathrm{rms}} = 7$ is reached at a streamwise location of $x/c \simeq 0.63$ (see Fig. 7a). The computed u^+ profile at this location shows a good qualitative match with its experimental counterpart and, in particular, exhibits a plateau in the region $10 \leq y^+ \leq 30$, albeit less marked than in the experiment. Mislevy and Wang [43] showed that this plateau in the early stages of transition is due to the presence of an adverse pressure gradient by comparing fluctuation profiles in transitioning boundary layers subject to different adverse pressure gradients. The height at which the maximum fluctuation levels are reached is slightly lower in the computational results, at approximately $y^+ \simeq 30$, to be compared with the value of $y^+ \simeq 40$ obtained experimentally. The most noticeable discrepancy in shape is observed for the profiles around $x/c = 0.69$ (see Fig. 7b). At this location, the computed profile peaks well inside the boundary layer at $y^+ = 18$ and closer to the wall than the measured profile, which reaches its maximum at around $y^+ = 65$. The fluctuation profiles obtained from the computation collapse cleanly in the viscous sublayer, as should be the case with properly computed friction velocity values.

The progressive transition to a turbulent state can be observed in the time histories of the streamwise velocity signals shown in Fig. 8. The velocity histories are represented as a function of nondimensional time t/t_c, where $t_c = c/U_\infty$ is the freestream convection time over the airfoil. The first signal is measured at $x/c = 0.5$, the second is from inside the transition zone at $x/c = 0.63$, and the last plot is from the turbulent zone at $x/c = 0.85$. All three signals are measured at a height of approximately 15 wall units from the airfoil. Note that the vertical scale for the first and last signal is half that of the second signal, to show signal shapes more clearly. Indeed, the second signal is measured at the point at which maximum levels of rms fluctuations are observed in the boundary layer, as can be seen in Fig. 5. It is interesting to note that the signal measured in the laminar zone is quite irregular. The oscillations are fairly sinusoidal, but their amplitude varies strongly with time. Fluctuations are thus present before transition takes place, these perturbations only being amplified once the boundary layer becomes unstable.

A 2-D view of the ω_z vorticity field around the trailing edge of the airfoil, presented in Fig. 9a, gives a visual representation of the process of transition. The appearance of large-amplitude vortical disturbances is seen to take place very quickly at approximately 60–65% of the chord in this snapshot. The initially large spanwise vortical structures break down rapidly to form much smaller components, which can be seen in Figs. 9b and 9c. These views show snapshots of the streamwise vorticity ω_x, taken from the top and the side, respectively. Small vortical structures appear around $x/c \simeq 0.63$, farther downstream than the oscillations apparent in Fig. 9a, because the boundary-layer instability is initially two-dimensional and only progressively becomes three-dimensional once the end of the linear growth region is reached.

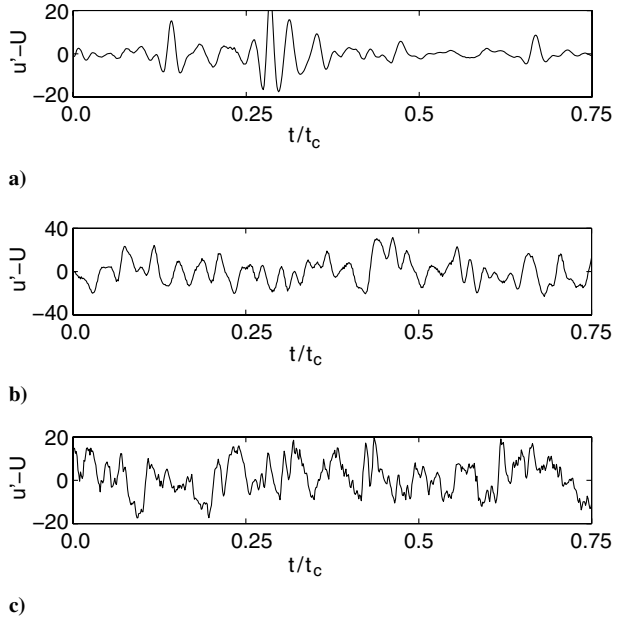

Fig. 8 Velocity signals in the boundary layer of the NACA 0012 airfoil at $Re_c = 5 \times 10^5$ and $M = 0.22$, measured at $y^+ \simeq 15$ and at different abscissae along the airfoil for x/c at a) 0.5, b) 0.63, and c) 0.85.

Vorticity is arranged in streamwise ribbons of alternating sign, for which the upstream ends are very close to the wall and the downstream ends are higher up in the boundary layer. The average observed length of the vortices varies from around $x^+ = 200$ at $x/c = 0.7$ to approximately $x^+ = 80$ at $x/c = 0.95$. They are commonly referred to as *horseshoe vortices* in the literature [42,44] and are generally believed to be responsible for the majority of turbulent energy creation in the boundary layer via their bursting process. Most of the horseshoe vortices observed are incomplete or one-sided, as also noted by Robinson [45] in his examination of DNS data obtained by Spalart [46] for a turbulent boundary layer. The average length of the horseshoe vortices observed in this work is comparable with that of $x^+ = 100$ given by Panton [42]. The average spanwise separation of these longitudinal structures in the computation is around $\Delta z^+ = 110$, which closely matches the value of $\Delta z^+ = 80$–100 found by Kline et al. [47].

C. Acoustic Results

The acoustic field generated by the airfoil is also captured in the computation. It is, moreover, properly propagated to the computational domain's outer boundaries, due to the low dispersion and low dissipation of the numerical technique used.

A preliminary examination of pressure-field snapshots shows them to be free from gross artifacts such as those sometimes induced by radiation conditions. This is promising, especially given the geometrical proximity of the radiation conditions to the acoustic source zone. Indeed, the radiation formulation used in this work is valid in the far field for a uniform mean flow [27]. Despite the distance from the trailing edge to the radiation conditions being of the same order as the airfoil chord, the far-field assumption is rather well-satisfied, because the acoustic source zone is concentrated at the trailing edge and the wavelengths of the acoustic radiation are small compared with the chord. However, the mean flow is clearly not uniform, particularly in the wake zone. The effect of the sponge zone can be noticed on the acoustic field shown in Fig. 10, in which acoustic waves seem to disappear in the downstream direction after $x/c \simeq 1.25$. This is due to the increased numerical dissipation in the sponge zone. Figure 10 also shows some slight reflections from the boundary conditions, but on the whole, they are deemed to be acceptable here in the context of the preliminary way in which acoustic levels are computed.

It should be noted that the convergence of the mean flowfield in the radiation zones during the initial transient phase of the computation is delicate: the rate at which the mean fields are adjusted with instantaneous information must approximately match the variation rate of these fields during the transient period.

Figure 10 shows an instantaneous view of the fluctuating pressure field around the airfoil. Sound waves can clearly be seen to radiate away from the trailing edge, the nearly circular aspect of these waves indicating that the emission zone is almost pointlike in the x–y plane. On this particular view, low-amplitude sound waves can also be seen to be leaving the leading edge. The upstream flow has no incoming artificial turbulence, and so it would appear that these waves are the result of the leading-edge diffracting waves emitted at the trailing edge. No particular frequency clearly dominates the sound field, as is supported by the narrow-band spectrum shown in Fig. 11. The plot represents the power spectral density, in decibels per Strouhal, of the fluctuating pressure at the edge of the computational domain. The coordinates of the measurement point are $x = 0.1$ and $y = 0.095$. The Strouhal number used here is based on the chord of the airfoil and the upstream flow velocity, $St_c = fc/U_\infty$. At the observation point, the Strouhal number resolution limit for acoustic waves is $St_c = 80$, based on a criterion of at least five points per wavelength. The

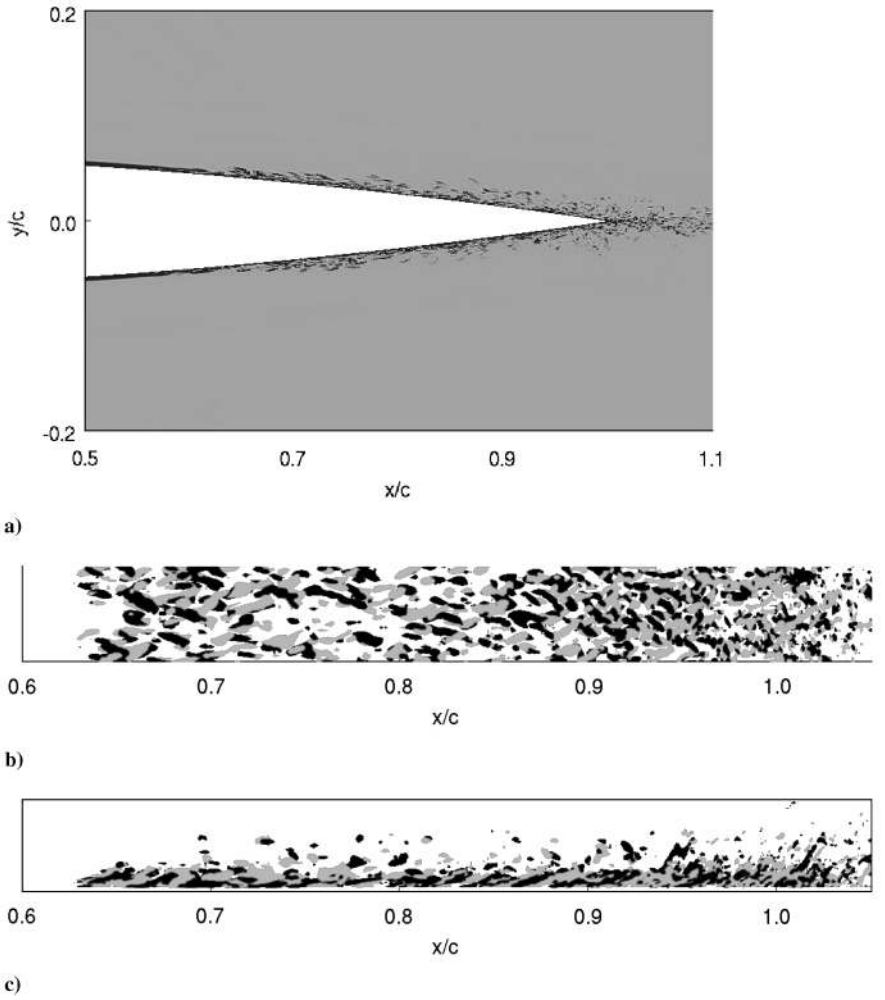

Fig. 9 Instantaneous views of the a) ω_z vorticity in the boundary layers around the trailing edge of a 3-D NACA 0012 airfoil at a Reynolds number of $Re_c = 5 \times 10^5$ and $M = 0.22$ (grayscale is between $\pm 1 \times 10^5$ s^{-1}), b) top view of the ω_x vorticity in the same boundary layer (gray and black surfaces correspond to $\pm 1.5 \times 10^5$ s^{-1}), and c) side view of the ω_x vorticity.

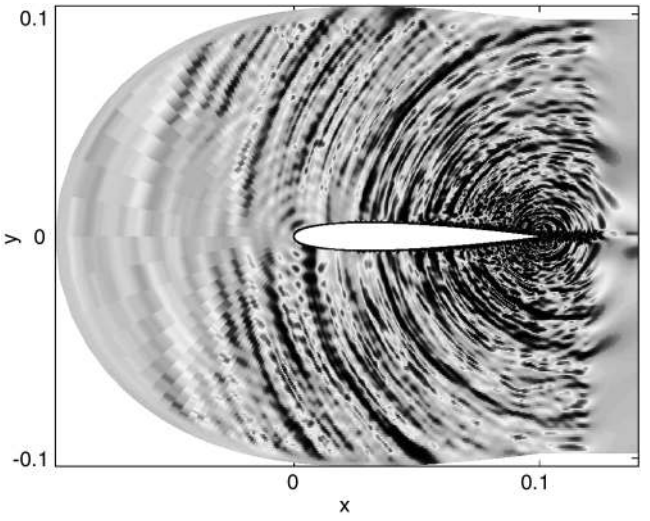

Fig. 10 Snapshot of the fluctuating pressure field around the NACA 0012 airfoil at $Re_c = 5 \times 10^5$ and $M = 0.22$ (grayscale is between −5 and 5 Pa).

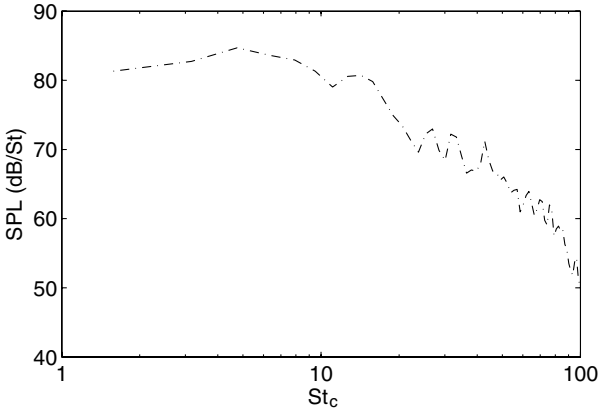

Fig. 11 Power spectral density in decibels per Strouhal of the fluctuating pressure at the edge of the computational domain.

acoustic emission is strongly broadband, with a notable level for Strouhal numbers lower than about 10. The maximum level is observed at a Strouhal number of approximately $St = 5$. The corresponding pressure signal, represented as a function of nondimensional time t/t_c, where t_c is the freestream convection time across the airfoil, is plotted in Fig. 12.

A quantitative comparison of acoustic results is made with experimental work from Brooks et al. [48]. Figure 13 shows the third-octave sound pressure level (SPL) as a function of frequency for the 10-cm airfoil of this computation, as well as for a 10.16-cm airfoil at a flow speed of 71.3 m/s. The experimental SPL was measured at a distance of 1.22 m from the airfoil above the trailing edge. The computational domain used in this work is obviously smaller than that, and so the pressure signal from the edge of the

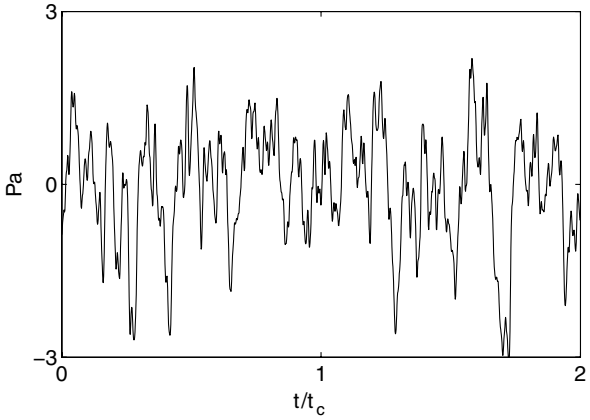

Fig. 12 Time history of the fluctuating pressure at the edge of the computational domain above the trailing edge of a NACA 0012 airfoil.

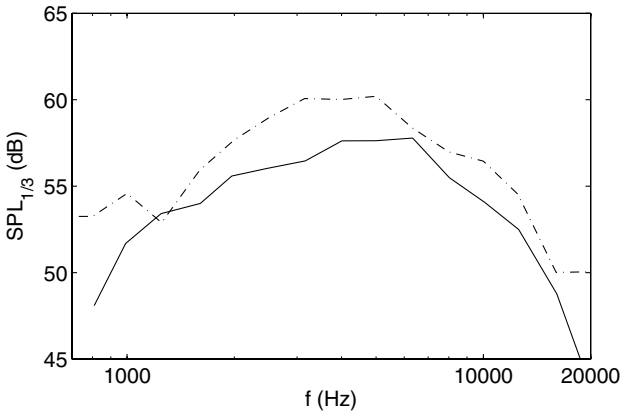

Fig. 13 Comparison of SPL in third-octave bands at 1.22 m from a NACA 0012 airfoil with results by Brooks et al. [48]: experimental results at $Re_c = 5 \times 10^5$ (solid line) and results from the computation (dotted–dashed line).

domain is taken and scaled, supposing that the radiation is of a two-dimensional nature in a uniform flow. The two spectra are observed to match well, with levels issued from the computation being slightly higher than experimental levels, but with differences not exceeding 3 dB. The simple scaling of pressure from a single point is a somewhat rough approximation and calls for a few remarks. Indeed, it first supposes that the flow from the computational measurement point (10 cm away from the trailing edge) outward to the experimental measurement point is uniform, which, judging from the computational results at the computational domain's boundaries, is a reasonable assumption. Furthermore, the simple scaling assumes that there is no diffraction from the leading edge of the airfoil back toward the measurement point, because only information on the direct propagation path from the trailing edge to the measurement point is used. This acoustic signal therefore does not contain the pressure fluctuations back-scattered by the leading edge toward the experimental measurement point, but contains the signal back-scattered toward the point at which the signal is measured in the computational domain. The assumption that the back-scattering is negligible at 90 deg to the trailing edge is especially true for higher frequencies; but, in any case, analytical studies of leading-edge back-scattering [49] suggest that this effect should remain marginal in the configuration studied here.

Supposing that the acoustic radiation is two-dimensional leads to an overestimation of the pressure level that is frequency-dependent, because the correlation length should depend on the frequency. Unfortunately, no experimental spanwise coherence data were provided by Lee and Kang [34] for their experiments. However, in the present simulation, once well outside the boundary layer, the pressure correlation across the domain's width is very high, on the order of 0.99, and hence the approximation should be sufficient to compare trends between experimental acoustic data and those obtained from the computation.

Unlike in experiments, it is not necessary to apply a correction to sound ray trajectories. Indeed, in experiments, sound propagating away from the airfoil is refracted by the shear layer of the experimental jet before reaching the microphone. This is not the case in the present simulation, because the flow covers the entire computational domain.

It can be noted that there is no indication of a strongly tonal Tollmien–Schlichting type acoustic radiation present in Fig. 13. This is in agreement with experimental observations by McAlpine et al. [50] for a NACA 0012 airfoil at a Reynolds number of 340,000 and at zero incidence to the flow. They observed a laminar-to-turbulent transition shortly upstream of the trailing edge and concluded that this transition broke any possible Tollmien–Schlichting feedback loop, thus precluding tonal noise.

IV. Conclusions

The flow around a 3-D NACA 0012 airfoil at a transitional chord-based Reynolds number of 500,000 and a Mach number of 0.22 was studied numerically with a parallel curvilinear compressible solver based on high-order methods. The airfoil is placed in a uniform mean flow at zero incidence to the direction of the flow. According to available experimental results, the airfoil's boundary layers at this Reynolds number are initially in a laminar state and transition toward turbulent boundary layers along the second half of the airfoil. The computational results presented in this work show that the location of the transition zone is well-captured and that the mean velocity field after the transition region is well-described by the modified turbulent logarithmic law, including adverse pressure gradient effects. Furthermore, rms velocity fluctuation profiles and skin-friction values are in reasonable agreement with experimental data. The acoustic field resulting from turbulent boundary-layer structures crossing the trailing edge is also determined in the same computation.

First analyses indicate that acoustic data follow expected trends. A broadband radiation pattern is observed, and no tonal Tollmien–Schlichting feedback loop is detected. A reasonable match is obtained between computational results and corresponding third-octave acoustic experimental spectra.

It is hoped in the near future to perform similar computations at different Mach numbers, allowing the comparison of the acoustic scaling with the analytical dependence on the fifth power of the velocity, which, to our knowledge, has not as yet been verified in compressible computations of turbulent flows crossing a trailing edge.

Appendix A: Navier–Stokes Equations in Curvilinear Coordinates

I. Curvilinear Equations

The geometrical transform between the physical domain and its computational counterpart is characterized by its Jacobian matrix, which describes the variations of the computational coordinates ξ, η, and ζ as a function of the physical coordinates x, y, and z, is given by

$$J = \begin{vmatrix} \frac{\partial \xi}{\partial x} & \frac{\partial \eta}{\partial x} & \frac{\partial \zeta}{\partial x} \\ \frac{\partial \xi}{\partial y} & \frac{\partial \eta}{\partial y} & \frac{\partial \zeta}{\partial y} \\ \frac{\partial \xi}{\partial z} & \frac{\partial \eta}{\partial z} & \frac{\partial \zeta}{\partial z} \end{vmatrix}$$

The transformed equations can be written as follows [51]:

$$\frac{\partial}{\partial t}\left(\frac{\mathbf{U}}{J}\right) + \frac{\partial}{\partial \xi}\left\{\frac{1}{J}[\xi_x(\mathbf{E_e}-\mathbf{E_v}) + \xi_y(\mathbf{F_e}-\mathbf{F_v}) + \xi_z(\mathbf{G_e}-\mathbf{G_v})]\right\} + \frac{\partial}{\partial \eta}\left\{\frac{1}{J}[\eta_x(\mathbf{E_e}-\mathbf{E_v}) + \eta_y(\mathbf{F_e}-\mathbf{F_v}) + \eta_z(\mathbf{G_e}-\mathbf{G_v})]\right\} + \frac{\partial}{\partial \zeta}\left\{\frac{1}{J}[\zeta_x(\mathbf{E_e}-\mathbf{E_v}) + \zeta_y(\mathbf{F_e}-\mathbf{F_v}) + \zeta_z(\mathbf{G_e}-\mathbf{G_v})]\right\} = 0 \quad \text{(A1)}$$

where

$$\mathbf{U} = (\rho, \rho u, \rho v, \rho w, \rho e_t)^T \tag{A2}$$

and the inviscid and viscothermal fluxes are given, respectively, by

$$\mathbf{E_e} = \begin{pmatrix} \rho u \\ \rho u^2 + p \\ \rho uv \\ \rho uw \\ (\rho e_t + p)u \end{pmatrix} \quad \mathbf{E_v} = \begin{pmatrix} 0 \\ \tau_{xx} \\ \tau_{xy} \\ \tau_{xz} \\ u\tau_{xx} + v\tau_{xy} + w\tau_{xz} - q_x \end{pmatrix}$$

$$\mathbf{F_e} = \begin{pmatrix} \rho v \\ \rho uv \\ \rho v^2 + p \\ \rho vw \\ (\rho e_t + p)v \end{pmatrix} \quad \mathbf{F_v} = \begin{pmatrix} 0 \\ \tau_{xy} \\ \tau_{yy} \\ \tau_{yz} \\ u\tau_{xy} + v\tau_{yy} + w\tau_{yz} - q_y \end{pmatrix}$$

$$\mathbf{G_e} = \begin{pmatrix} \rho w \\ \rho uw \\ \rho vw \\ \rho w^2 + p \\ (\rho e_t + p)w \end{pmatrix} \quad \mathbf{G_v} = \begin{pmatrix} 0 \\ \tau_{xz} \\ \tau_{yz} \\ \tau_{zz} \\ u\tau_{xz} + v\tau_{yz} + w\tau_{zz} - q_z \end{pmatrix}$$

Subscripts denote partial differentiation with respect to the subscripted variable (i.e., $u_\xi = \partial u/\partial \xi$). The shear stress terms are given by the following expressions:

$$\begin{aligned}
\tau_{xx} &= \tfrac{2}{3}\mu[2(\xi_x u_\xi + \eta_x u_\eta + \zeta_x u_\zeta) - (\xi_y v_\xi + \eta_y v_\eta + \zeta_y v_\zeta) \\
&\quad - (\xi_z w_\xi + \eta_z w_\eta + \zeta_z w_\zeta)] \\
\tau_{yy} &= \tfrac{2}{3}\mu[2(\xi_y v_\xi + \eta_y v_\eta + \zeta_y v_\zeta) - (\xi_x u_\xi + \eta_x u_\eta + \zeta_x u_\zeta) \\
&\quad - (\xi_z w_\xi + \eta_z w_\eta + \zeta_z w_\zeta)] \\
\tau_{zz} &= \tfrac{2}{3}\mu[2(\xi_z w_\xi + \eta_z w_\eta + \zeta_z w_\zeta) - (\xi_x u_\xi + \eta_x u_\eta + \zeta_x u_\zeta) \\
&\quad - (\xi_y v_\xi + \eta_y v_\eta + \zeta_y v_\zeta)] \\
\tau_{xy} &= \mu(\xi_y u_\xi + \eta_y u_\eta + \zeta_y u_\zeta + \xi_x v_\xi + \eta_x v_\eta + \zeta_x v_\zeta) \\
\tau_{xz} &= \mu(\xi_z u_\xi + \eta_z u_\eta + \zeta_z u_\zeta + \xi_x w_\xi + \eta_x w_\eta + \zeta_x w_\zeta) \\
\tau_{yz} &= \mu(\xi_z v_\xi + \eta_z v_\eta + \zeta_z v_\zeta + \xi_y w_\xi + \eta_y w_\eta + \zeta_y w_\zeta) \\
q_x &= -k(\xi_x T_\xi + \eta_x T_\eta + \zeta_x T_\zeta) \\
q_y &= -k(\xi_y T_\xi + \eta_y T_\eta + \zeta_y T_\zeta) \\
q_z &= -k(\xi_z T_\xi + \eta_z T_\eta + \zeta_z T_\zeta)
\end{aligned}$$

where the heat flux terms q_x, q_y, and q_z are obtained using Fourier's law:

$$\mathbf{q} = -k\nabla T$$

where $k = \mu c_p/\sigma$ (μ is the dynamic molecular viscosity specified by Sutherland's law, c_p is the specific heat at constant pressure, and σ is Prandtl's number, for which the value is generally set to 0.72 for typical airflows).

II. Wall Condition

At a hard surface, velocity components are equal to zero and do not need to be updated. The equations governing density and total energy are also simplified by the zero velocity at the wall. For instance, for a wall described by $\eta = 0$, the density equation thus becomes

$$\frac{\partial \rho}{\partial t} = \frac{\partial}{\partial \eta}\left\{\frac{1}{J}\left[\frac{\partial \eta}{\partial x}\rho u + \frac{\partial \eta}{\partial y}\rho v\right]\right\}$$

The right-hand spatial derivatives are computed using the one-sided 11-point differencing scheme for which the details are presented in Berland et al. .

Acknowledgments

This study was undertaken as part of a doctoral work financially supported by Electricité de France (EDF), under the guidance of P. Lafon, and the Centre National de Recherche Scientifique (CNRS). Some of the computations used in this work were performed using computing resources supplied by the Institut du Dévelopement et des Resources en Informatique Scientifique (IDRIS), as well by the Centre d'Etudes Atomiques (CEA).

References

[1] Tam, C. K. W., and Webb, J. C., "Dispersion-Relation-Preserving Finite Difference Schemes for Computational Acoustics," *Journal of Computational Physics*, Vol. 107, No. 2, 1993, pp. 262–281. doi:10.1006/jcph.1993.1142

[2] Bogey, C., and Bailly, C., "A Family of Low Dispersive and Low Dissipative Explicit Schemes for Noise Computations," *Journal of Computational Physics*, Vol. 194, No. 1, 2004, pp. 194–214. doi:10.1016/j.jcp.2003.09.003

[3] Lele, S. K., "Compact Finite Difference Schemes with Spectral-Like Resolution," *Journal of Computational Physics*, Vol. 103, Nov. 1992, pp. 16–42. doi:10.1016/0021-9991(92)90324-R

[4] Visbal, M., and Gaitonde, D., "High-Order-Accurate Methods for Complex Unsteady Subsonic Flows," *AIAA Journal*, Vol. 37, No. 10, 1999, pp. 1231–1239.

[5] Bogey, C., Bailly, C., and Juvé, D., "Noise Investigation of a High Subsonic, Moderate Reynolds Number Jet Using a Compressible LES," *Theoretical and Computational Fluid Dynamics*, Vol. 16, No. 4, 2003, pp. 273–297. doi:10.1007/s00162-002-0079-4

[6] Bogey, C., and Bailly, C., "Investigation of Downstream and Sideline Subsonic Jet Noise Using Large Eddy Simulations," *Theoretical and Computational Fluid Dynamics*, Vol. 20, No. 1, 2006, pp. 23–40. doi:10.1007/s00162-005-0005-7

[7] Bodony, D. J., and Lele, S. K., "On Using Large-Eddy Simulation for the Prediction of Noise from Cold and Heated Turbulent Jets," *Physics of Fluids*, Vol. 17, No. 085103-1, 2005. doi:10.1063/1.2001689

[8] Uzun, A., Lyrintzis, A. S., and Blaisdell, G. A., "Coupling of Integral Acoustics Methods with LES for Jet Noise Prediction," *International Journal of Aeroacoustics*, Vol. 3, No. 4, Oct. 2004, pp. 297–346. doi:10.1260/1475472043499290

[9] Visbal, M., and Gaitonde, D., "Very High-Order Spatially Implicit Schemes for Computational Acoustics on Curvilinear Meshes," *Journal of Computational Acoustics*, Vol. 9, No. 4, 2000, pp. 1259–1286. doi:10.1142/S0218396X01000541

[10] Manoha, E., Herrero, C., Sagaut, P., and Redonnet, S., "Numerical Prediction of Airfoil Aerodynamic Noise," AIAA Paper 2002-2573, 2002.

[11] Visbal, M., and Gaitonde, D., "On the Use of Higher-Order Finite Difference Schemes on Curvilinear and Deforming Meshes," *Journal of Computational Physics*, Vol. 181, Sept. 2002, pp. 155–185. doi:10.1006/jcph.2002.7117

[12] Marsden, O., Bogey, C., and Bailly, C., "High-Order Curvilinear Simulations of Flows Around Noncartesian Bodies," *Journal of Computational Acoustics*, Vol. 13, No. 4, 2005. doi:10.1142/S0218396X05002906

[13] Wang, M., and Moin, P., "Computation of Trailing-Edge Flow and Noise Using Large-Eddy Simulation," *AIAA Journal*, Vol. 38, No. 12, 2000, pp. 2201–2209.

[14] Oberai, A., Roknaldin, F., and Hughes, Th., "Computation of Trailing-Edge Noise Due to Turbulent Flow over an Airfoil," *AIAA Journal*, Vol. 40, No. 11, 2002, pp. 2206–2216.

[15] Kim, H.-J., Lee, S., and Fujisawan, N., "Computation of Unsteady Flow and Aerodynamic Noise of NACA0018 Airfoil Using Large-Eddy Simulation," *International Journal of Heat and Fluid Flow*, Vol. 27, No. 2, 2006, pp. 229–242. doi:10.1016/j.ijheatfluidflow.2005.08.007

[16] Nagarajan, S., Hahn, S., and Lele, S., "Prediction of Sound Generated by a Pitching Airfoil: A Comparison of RANS and LES," AIAA Paper 2006-2516, 2006.

[17] Ffowcs Williams, J. E., and Hall, L. H., "Aerodynamic Sound Generation by Turbulent Flow in the Vicinity of a Scattering Half-Plane," *Journal of Fluid Mechanics*, Vol. 40, No. 4, Mar. 1970, pp. 657–670. doi:10.1017/S0022112070000368

[18] Blake, W. K., "A Statistical Description of Pressure and Velocity Fields at the Trailing Edge of a Flat Strut," David Taylor Naval Ship Research and Development Center, Rept. 4241, Bethesda, MD, Dec. 1975.

[19] Gloerfelt, X., Bailly, C., and Juvé, D., "Direct Computation of the Noise Radiated by a Subsonic Cavity Flow and Application of Integral Methods," *Journal of Sound and Vibration*, Vol. 266, No. 1, 2003, pp. 119–146. doi:10.1016/S0022-460X(02)01531-6

[20] Berland, J., Bogey, C., Marsden, O., and Bailly, C., "High-Order, Low Dispersive and Low Dissipative Explicit Schemes for Multiple-Scale and Boundary Problems," *Journal of Computational Physics*, Vol. 224, No. 2, June 2007, pp. 637–662. doi:10.1016/j.jcp.2006.10.017

[21] Visbal, M., and Rizzetta, D., "Large-Eddy Simulation on Curvilinear Grids Using Compact Differencing and Filtering Schemes," *Journal of Fluids Engineering*, Vol. 124, No. 4, 2002. doi:10.1115/1.1517564

[22] Rizzetta, D. P., Visbal, M. R., and Blaisdell, G. A., "A Time-Implicit High-Order Compact Differencing and Filtering Scheme for Large-Eddy Simulation," *International Journal for Numerical Methods in Fluids*, Vol. 42, June 2003, pp. 665–693. doi:10.1002/fld.551

[23] Bogey, C., and Bailly, C., "Effects Of Inflow Conditions and Forcing on a Mach 0.9 Jet and Its Radiated Noise," *AIAA Journal*, Vol. 43, No. 5, 2005, pp. 1000–1007.

[24] Bogey, C., and Bailly, C., "An Analysis of the Correlations Between the Turbulent Flow and the Sound Pressure Fields of Subsonic Jets," *Journal of Fluid Mechanics*, Vol. 583, 2007, pp. 71–97. doi:10.1017/S002211200700612X

[25] Gaitonde, D., and Visbal, M., "Padé-Type Higher-Order Boundary Filters for the Navier–Stokes Equations," *AIAA Journal*, Vol. 38, No. 11, Nov. 2000, pp. 2103–2112.

[26] Tam, C. K. W., and Dong, Z., "Radiation and Outflow Boundary Conditions for Direct Computation of Acoustic and Flow Disturbances In a Nonuniform Mean Flow," *Journal of Computational Acoustics*, Vol. 4, No. 2, 1996, pp. 175–201. doi:10.1142/S0218396X96000040

[27] Bogey, C., and Bailly, C., "Three-Dimensional Nonreflective Boundary Conditions for Acoustic Simulations: Far Field Formulation and Validation Test Cases," *Acta Acustica*, Vol. 88, No. 4, 2002, pp. 463–471; also available online at https://www.eaa-fenestra.org/Products/ActaAcustica/most_cited/acta_88_2002_Bogey.pdf.

[28] Hixon, R., Nallasamy, M., and Sawyer, S. D., "Parallelization Strategy for an Explicit Computational Aeroacoustics Code," AIAA Paper 2002-2583, 2002.

[29] Dahlström, S., and Davidson, L., "Large Eddy Simulation of the Flow Around an Airfoil," AIAA Paper 2001-0425, 2001.

[30] Davidson, L., Cokljat, D., Fröhlich, J., Leschziner, M. A., Mellen, C., and Rodi, W., *LESFOIL: Large Eddy Simulation of the Flow Around a High-Lift Airfoil*, Notes on Numer. Fluid Mech., Vol. 83, Springer, New York, 2003.

[31] Mellen, C., Fröhlich, J., and Rodi, W., "Lessons from the European LESFOIL Project on LES of Flow Around an Airfoil," AIAA Paper 2002-0111, 2002.

[32] Falkner, V. M., and Skan, W., "Some Approximate Solutions of the Boundary Layer Equations," Aeronautical Research Council Reports and Memoranda No. 1314, London, 1930.

[33] Clauser, F. H., "Turbulent Boundary Layers in Adverse Pressure Gradients," *Journal of the Aeronautical Sciences*, Vol. 21, No. 2, 1954, pp. 91–108.

[34] Lee, H. K., and Kang, S. H., "Flow Characteristics of Transitional Boundary Layers on an Airfoil in Wakes," *Journal of Fluids Engineering*, Vol. 122, No. 3, Sept. 2000, pp. 522–532. doi:10.1115/1.1287592

[35] Evans, R. L., "Freestream Turbulence Effects on Turbulent Boundary Layers in Adverse Pressure Gradients," *AIAA Journal*, Vol. 23, No. 11, 1985, pp. 1814–1816.

[36] Hoffman, J. A., Kassir, S. M., and Larwood, S. M., "The Influence of Freestream Turbulence on Turbulent Boundary Layers with Mild Adverse Pressure Gradients," NASA CR 177520, 1989.

[37] Kerho, M. F., and Bragg, M. B., "Airfoil Boundary-Layer Development and Transition with Large Leading-Edge Roughness," *AIAA Journal*, Vol. 35, No. 1, 1997.

[38] Silverstein, A., and Becker, J. V., "Determination of the Boundary-Layer Transition on Three Symmetrical Airfoils in the N.A.C.A. Full-Scale Wind Tunnel," NACA, TR 637, 1938.

[39] Gartenberg, E., and Roberts, A. S., Jr., "Airfoil Transition and Separation Studies Using an Infrared Imaging System," *Journal of Aircraft*, Vol. 28, No. 4, 1991, pp. 225–230.

[40] Afzal, N., "Wake Layer in a Turbulent Boundary Layer with Pressure Gradient: A New Approach," *IUTAM Symposium on Asymptotic Methods for Turbulent Shear Flows at High Reynolds Numbers*, edited by K. Gersten, Kluwer Academic, Norwell, MA, 1996.

[41] Schlichting, H., *Boundary Layer Theory*, McGraw–Hill, New York, 1968.

[42] Panton, R. L., "Overview of the Self-Sustaining Mechanisms of Wall Turbulence," *Progress in Aerospace Sciences*, Vol. 37, No. 4, 2001, pp. 341–383. doi:10.1016/S0376-0421(01)00009-4

[43] Mislevy, S. P., and Wang, T., "The Effects of Adverse Pressure Gradients on Momentum and Thermal Structures in Transitional Boundary Layers, Part 2: Fluctuation Quantities," *Journal of Turbomachinery*, Vol. 118, No. 4, Oct. 1996, pp. 728–732.

[44] Theodorsen, T., "Mechanism of Turbulence," *Proceedings of the Second Midwestern Conference on Fluid Mechanics*, Ohio State Univ., Columbus, OH, 1952, pp. 1–18.

[45] Robinson, S. K., "Coherent Motions in the Turbulent Boundary Layer," *Annual Review of Fluid Mechanics*, Vol. 23, 1991. doi:10.1146/annurev.fl.23.010191.003125

[46] Spalart, P. R., "Direct Simulation of a Turbulent Boundary Layer up to $R_\theta = 1410$," *Journal of Fluid Mechanics*, Vol. 187, 1988, pp. 61–98. doi:10.1017/S0022112088000345

[47] Kline, S. J., Reynolds, W. C., Schraub, F. A., and Runstadler, P. W., "The Structure of Turbulent Boundary Layers," *Journal of Fluid Mechanics*, Vol. 30, Dec. 1967, pp. 741–773. doi:10.1017/S0022112067001740

[48] Brooks, T., Pope, S., and Marcolini, M., "Airfoil Self-Noise and Prediction," NASA TR 1218, July 1989.

[49] Roger, M., Moreau, S., and Wang, M., "An Analytical Model for Predicting Airfoil Self-Noise Using Wall Pressure Statistics," *Annual Research Briefs*, Center for Turbulence Research, Stanford Univ., Stanford, Ca, 2002.

[50] McAlpine, A., Nash, E. C., and Lowson, M. V., "On the Generation of Discrete Tones by the Flow Around an Aerofoil," *Journal of Sound and Vibration*, Vol. 222, No. 5, 1999, pp. 753–779. doi:10.1006/jsvi.1998.2085

[51] Anderson, D. A., Tannehill, J. C., and Pletcher, R. H., *Computational Fluid Mechanics and Heat Transfer*, Hemisphere, New York, 1984.

D. Gaitonde
Associate Editor